Supplementary Material for "Local-nonlinearity-enabled Deep Sub-diffraction Control of Acoustic Waves"

Jiaxin Zhong[*1,2], Chengbo Hu[*1], Kangkang Wang[1], Jun Ji[2], Tao Zhuang[1], Haishan Zou[1], Jing Lu[1], Hyeonu Heo[2], Bin Liang[†1], Yun Jing[‡2], and Jian-Chun Cheng[§1]

[1]Key Laboratory of Modern Acoustics and Institute of Acoustics, Nanjing University, Nanjing 210093, China

[2]Graduate Program in Acoustics, The Pennsylvania State University, University Park, PA 16802, USA

October 31, 2023

Contents

[*]These two authors contributed equally

[†]liangbin@nju.edu.cn

[‡]jing.yun@psu.edu

[§]jccheng@nju.edu.cn

1 The extended second-order nonlinear equation

In a homogeneous and viscous fluid such as air, the acoustic wave with finite amplitude is governed by the extended second-order nonlinear wave equation [1, 2]

$$\left(\boldsymbol{\nabla}^2 - \frac{1}{c_0^2}\frac{\partial^2}{\partial t^2}\right)p + \frac{\delta}{c_0^4}\frac{\partial^3 p}{\partial t^3} - \frac{2}{\pi c_0^2}\sum_{\nu=1}^{\mathcal{N}}(\alpha_\nu\lambda)_{\mathrm{max}}\frac{\partial^2 p_\nu}{\partial t^2} = -\frac{\beta}{\rho_0 c_0^4}\frac{\partial^2 p^2}{\partial t^2} - \left(\boldsymbol{\nabla}^2 + \frac{1}{c_0^2}\frac{\partial^2}{\partial t^2}\right)\mathcal{L}, \tag{S1}$$

where $p = p(\mathbf{r}, t)$ is the sound pressure at the time t and an observation point $\mathbf{r} = (x, y)$, ρ_0 is the air density, and c_0 is the speed of sound of linear acoustics. The second term on the left-hand side accounts for the classical thermoviscosity, where $\delta = \left[4\mu_{\mathrm{s}}/3 + \mu_{\mathrm{b}} + \kappa(c_{\mathrm{V}}^{-1} - c_{\mathrm{P}}^{-1})\right]/\rho_0$ is the sound diffusivity, μ_{s} and μ_{b} are the shear and bulk viscosity, respectively, κ is the coefficient of thermal conduction, c_{P} and c_{V} are the specific heats at constant pressure and volume, respectively. The third term on the left-hand side represents the relaxation effects of $\mathcal{N}$ molecules in air (e.g., nitrogen and oxygen), where $(\alpha_\nu\lambda)_{\mathrm{max}}$ is the maximum absorption per wavelength due to relaxation effects from the ν-th molecule, $p_\nu = p_\nu(\mathbf{r}, t)$ is the solution of the equation $\partial p_\nu/\partial t + (p_\nu - p)/\tau_\nu = 0$ associated with the ν-th molecule [2, 3], and τ_ν is the relaxation time. For the harmonic sound field investigated in this work, the dissipative process including the classical thermoviscosity and relaxation can be simplified by considering a complex wavenumber $k_i = \omega_i/c_0 + \mathrm{i}\alpha(\omega_i)$, with $\omega_i = 2\pi f_i$ being the angular frequency, and $i = 1, 2$ being the index for numbering the ultrasound sources. The sound absorption coefficient is $\alpha(\omega) = \delta\omega^2/(2c_0^3) + \sum_{\nu=1}^{\mathcal{N}}\frac{(\alpha_\nu\lambda)_{\mathrm{m}}}{\pi c_0}\frac{\omega^2\tau_\nu}{1+(\omega\tau_\nu)^2}$ [3]. The terms on the right-hand side of Eq. (S1) account for the second-order nonlinear effects, where $\beta = 1.2$ is the nonlinearity coefficient of air, $\mathcal{L} = \mathcal{L}(\mathbf{r}, t) = \rho_0\mathbf{v}\cdot\mathbf{v}/2 - p^2/(2\rho_0 c_0^2)$ represents the Lagrangian density [1, 4, 5], and $\mathbf{v} = \mathbf{v}(\mathbf{r}, t)$ is the particle velocity.

To gain analytical insights into the nonlinear interaction of acoustic waves, we use the quasilinear approximation and successive method, whereby Eq. (S1) can be decomposed into two coupled linear wave equations. Under this framework, the ultrasound field is approximated by its solution satisfying the linear Helmholtz equation, [1, 4, 5].

$$\left(\boldsymbol{\nabla}^2 + k_i^2\right)p_i = 0, \tag{S2}$$

where p_i is the ultrasound pressure field at the frequency of f_i.

For the physical model shown in Fig. 1 of the paper, the ultrasound field can be modeled as the radiation from a baffled line source, so that the ultrasound pressure at the frequency f_i is [6]

$$p_i(\mathbf{r}) = \frac{p_0}{2}\int_S u_i(\mathbf{r}_{\mathrm{s}})H_0^{(1)}(k_i|\mathbf{r} - \mathbf{r}_{\mathrm{s}}|)k_i\mathrm{d}S, \tag{S3}$$

where $p_0 = \rho_0 c_0 v_0$ is the on-surface sound pressure amplitude, v_0 is the amplitude of the vibration velocity, $H_0^{(1)}(\cdot)$ is the first-kind Hankel function of order zero, $\mathbf{r}_{\mathrm{s}} = (x_{\mathrm{s}}, y_{\mathrm{s}})$ is the source point on the radiation surface S, $\mathbf{n}_{\mathrm{s}}$ is the normal direction of the radiation surface, and the harmonic term $\exp(-\mathrm{i}\omega_i t)$ is omitted for simplicity. To enable the focusing at a point $\mathbf{r}_{\mathrm{f}} = (x_{\mathrm{f}}, y_{\mathrm{f}})$, the velocity profile can take the form of $u_i(\mathbf{r}_{\mathrm{s}}) = \exp(-\mathrm{i}\Re k_i|\mathbf{r}_{\mathrm{s}} - \mathbf{r}_{\mathrm{f}}|)$, where $\Re$ takes the real part. In this work, however, the focusing is achieved by placing a phase mask in front of the source, which is detailed in the paper.

The particle velocity can be obtained by using the linear relation between the acoustic pressure and particle velocity, i.e., $\mathbf{v}_i = \mathrm{i}\rho_0\omega_i\boldsymbol{\nabla}p_i$, which has the form of

$$\begin{cases} v_{i,x}(\mathbf{r}) = \dfrac{\mathrm{i}v_0}{2}\displaystyle\int_S u_i(\mathbf{r}_{\mathrm{s}})\dfrac{k_i(x - x_{\mathrm{s}})}{|\mathbf{r} - \mathbf{r}_{\mathrm{s}}|}H_1^{(1)}(k_i|\mathbf{r} - \mathbf{r}_{\mathrm{s}}|)\mathrm{d}S, \\[2ex] v_{i,y}(\mathbf{r}) = \dfrac{\mathrm{i}v_0}{2}\displaystyle\int_S u_i(\mathbf{r}_{\mathrm{s}})\dfrac{k_i(y - y_{\mathrm{s}})}{|\mathbf{r} - \mathbf{r}_{\mathrm{s}}|}H_1^{(1)}(k_i|\mathbf{r} - \mathbf{r}_{\mathrm{s}}|)\mathrm{d}S, \end{cases} \tag{S4}$$

where $H_1^{(1)}(\cdot)$ is the first-kind Hankel function of first order.

It is important to point out that, our proposed wave control technique, which relies on local nonlinearity, distinguishes itself from the conventional parametric array [7]. Parametric arrays operate by emitting two intense primary waves at distinct frequencies, resulting in the *cumulative* nonlinear generation of a directional difference frequency wave [8]. The term "parametric" originates from the parameter of nonlinearity, denoted as β, in the nonlinear wave equation [9]. Specifically, it refers to the first term (highlighted in purple) on the right-hand side of Eq. (S1). In Westervelt's seminal paper introducing the concept of the parametric array, the governing equation is the Westervelt equation [8]. However, in the Westervelt equation, the second term (highlighted in red) on the right-hand side of Eq. (S1) is omitted (i.e., $\mathcal{L} = 0$), indicating that the Westervelt equation does not incorporate local nonlinearity. This omission is justifiable because in a parametric array, the two primary waves are collinear, causing local nonlinear effects to be typically negligible when compared to cumulative nonlinear effects. This is due to the quasi-planar relationship between sound pressure and particle velocity, expressed as $p \approx \rho_0 c_0 v$.

Consequently, the primary distinction in the underlying physical mechanisms between the parametric antenna and our research lies in the fact that the parametric antenna relies on cumulative nonlinearity, whereas our approach to deep sub-diffraction control of acoustic waves hinges on local nonlinearity. In our work, the utilization of two crossed primary beams serves to largely mitigate cumulative nonlinear effects while amplifying local nonlinear effects. Our investigation underscores the critical role of local nonlinear effects in achieving super-resolution focusing.

To elucidate further, even when the nonlinear coefficient is zero (i.e., $\beta = 0$), Eq. (S1) remains a nonlinear wave equation because the Lagrangian density encompasses the square of both the pressure and velocity fields, i.e., $\mathcal{L} = \rho_0 \mathbf{v} \cdot \mathbf{v}/2 - p^2/(2\rho_0 c_0^2)$. This observation underscores that local nonlinearity operates independently of medium nonlinearity, which represents cumulative nonlinearity. Therefore, our proposed method constitutes a fundamentally novel approach to circumventing the linear diffraction limit, as opposed to relying on the parametric array technique.

2 Parameters of the designed phase masks

FIgure S1 presents the geometric parameters, transmitted phase, and amplitude of each unit cell for the designed phase masks. The phase distributions of both masks were obtained using the iterative angular spectrum approach [10]. Next, the scale factor γ and transmitted amplitude were determined according to Fig. 2(d) in the paper.

3 Performance of the designed phase masks at different frequencies

The phase masks employed in this study were designed to operate at a center frequency of 25 kHz. However, numerical simulations conducted using COMSOL shown in Fig. S2 demonstrate that the one-focal-point and two-focal-point focusing perform effectively across a wide bandwidth. In Fig. S2, the top row shows 2D pressure distributions generated by a one-focal-point phase mask placed on the left, at four different ultrasound frequencies ranging from 24.5 to 25 kHz. The bottom row displays the 2D pressure distributions generated by a two-focal-point phase mask placed on the bottom, at four different ultrasound frequencies ranging from 25 to 25.5 kHz. These results suggest that the designed phase masks enable deep sub-diffraction acoustic imaging based on the local nonlinearity at a difference-frequency of up to 1 kHz (corresponding to a bandwidth of 4% with respect to the ultrasound frequency of 25 kHz).
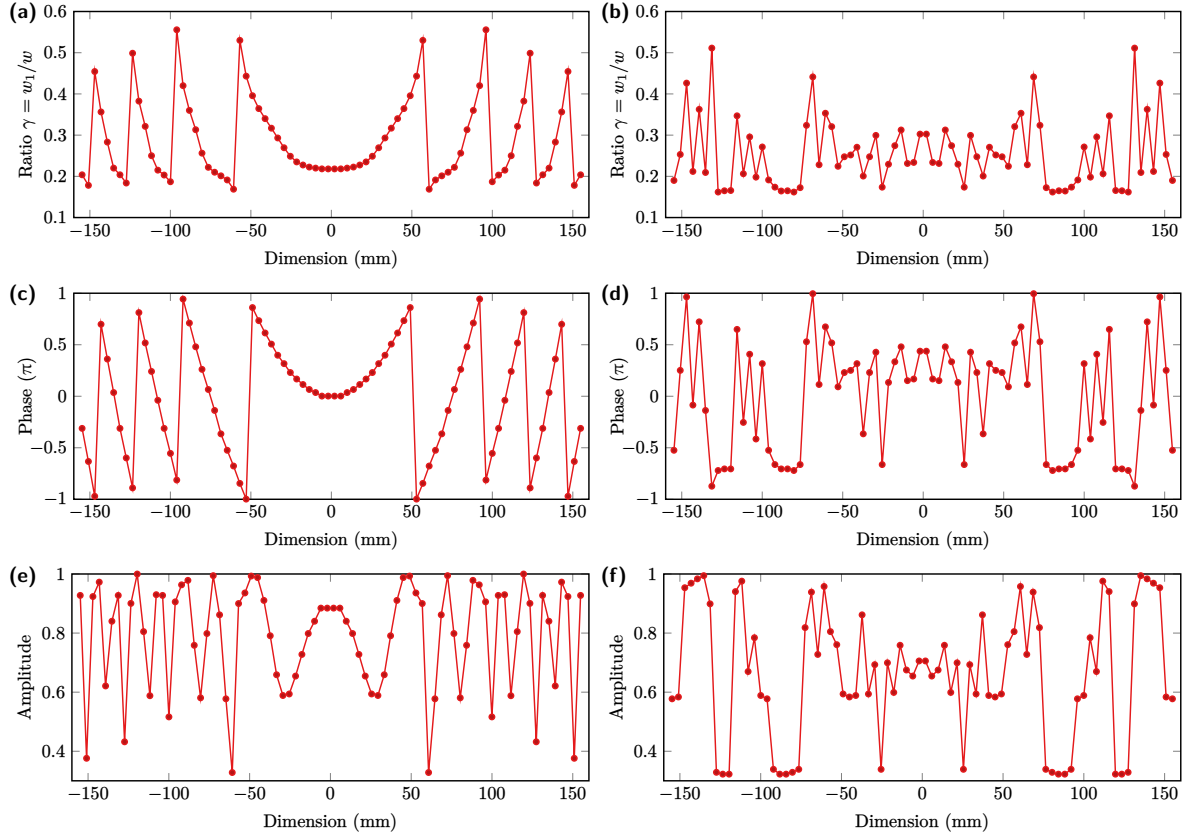
Figure S1: Parameters of the designed phase masks used in this work, where the horizontal axes correspond to the location of the units. Top row, the geometric ratio γ; middle row, the transmitted phase at 25 kHz; bottom row, the transmitted amplitude at 25 kHz. Left column, the phase mask placed on the left for generating a one-focal-point ultrasound field; right column, the phase mask placed on the bottom for generating a two-focal-point ultrasound field.

Notably, this bandwidth represents a bandwidth of 500% with respect to the difference-frequency of 200 Hz.
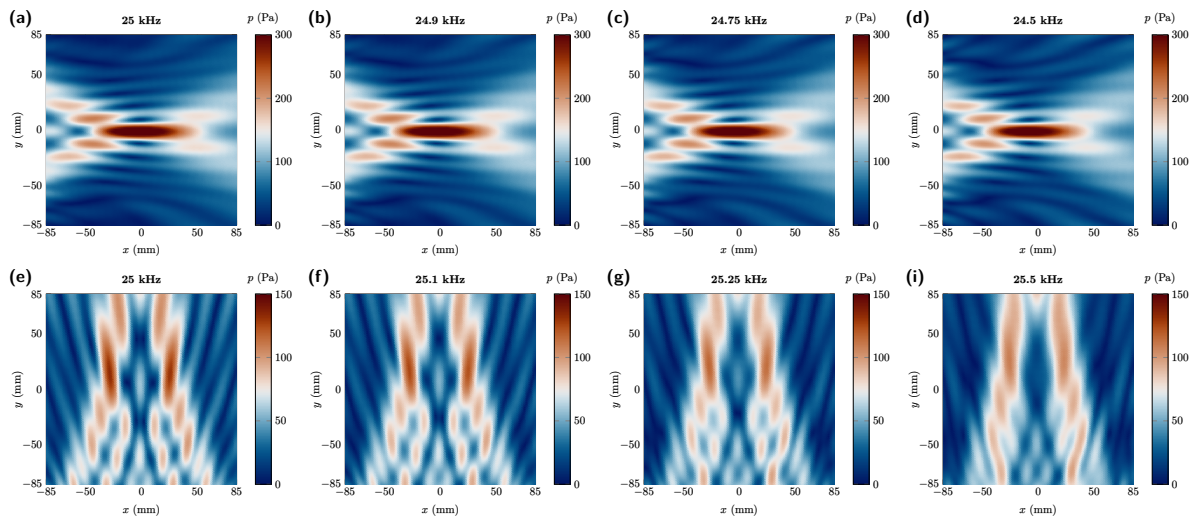

Figure S2: The 2D pressure distributions calculated by COMSOL at different frequencies. Top row, the the one-focal-point ultrasound field generated by a same phase mask placed on the left; Bottom row, the two-focal-point ultrasound field generated by a same phase mask placed on the bottom.

4 Linear acoustics focusing

In this section, a line source with a same size of $2a = 331.6\,\text{mm}$ is assumed to be placed at $x = -200\,\text{mm}$. In linear acoustics, the velocity profile for generating two focal points takes the form of

$$u(\mathbf{r}_\text{s}) = \exp\left(-\text{i}k|\mathbf{r}_\text{s} - \mathbf{r}_{\text{f},1}|\right) + \exp\left(-\text{i}k|\mathbf{r}_\text{s} - \mathbf{r}_{\text{f},2}|\right), \tag{S5}$$

where $\mathbf{r}_{\text{f},1} = (0, -25\,\text{mm})$ and $\mathbf{r}_{\text{f},2} = (0, 25\,\text{mm})$ are the coordinates of two focal points.

The radiated sound field at the frequency of f can be calculated by [11]

$$p(\mathbf{r}) = \frac{p_0}{2} \int_S u(\mathbf{r}_\text{s}) H_0^{(1)}(k|\mathbf{r} - \mathbf{r}_\text{s}|) k\mathbf{n}_\text{s} \cdot \text{d}\mathbf{r}_\text{s}, \tag{S6}$$

which is similar to Eq. (S3), while the wavenumber is replaced by $k = 2\pi f / c_0$.

The 2D pressure distributions of the audio sound resulting from linear acoustics focusing at 200 Hz, 300 Hz, 400 Hz, and 500 Hz are displayed in Fig. S3. No focal beams are observed in Fig. S3. This can be attributed to the small size of the source (331.6 mm) compared to the wavelength (e.g., 1715 mm at 200 Hz), causing the sound source to behave like a monopole. However, in Figs. 3(c) and 4(d-e) of the paper, it is demonstrated that deep sub-diffraction acoustic imaging can be achieved using local nonlinear effects even with a source of the same size.
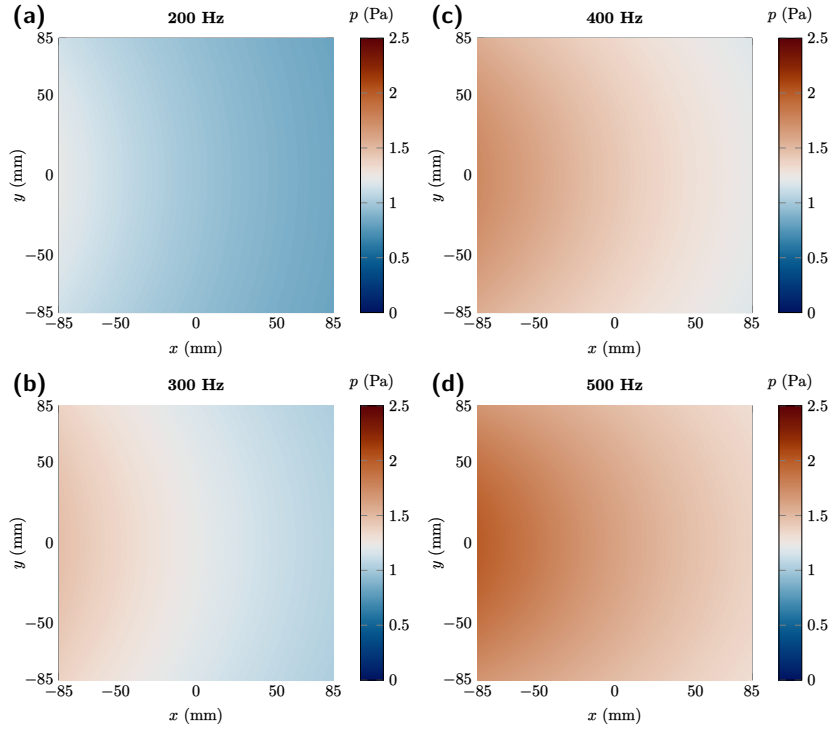

Figure S3: The 2D pressure distributions of the audio sound resulted from the linear acoustics focusing calculated by MATLAB using Eq. (S6). The line source has a dimension of 331.6 mm and its center is located at $(-200\,\text{mm}, 0)$. (a) 200 Hz, (b) 300 Hz, (c) 400 Hz, and (d) 500 Hz.

5 Local-nonlinearity-based deep subwavelength focusing by optimizing both amplitude and phase distributions of sources

5.1 Performance at different DFW frequencies with the focal distance set to $D = 0.2\,\mathrm{m}$

The spurious lobe presenting at the origin, as seen in Fig. 3(b) of the paper, when employing the proposed local nonlinearity-based technique, is a consequence of the limitations inherent in the phase mask utilized in this study. This phase mask, as it stands, permits adjustments solely to the phase component. This spurious lobe could potentially be eliminated if we had the capability to tune both the amplitude and phase of the ultrasound source. To demonstrate this, we have provided simulation results in Fig. S4. In this case, the bottom ultrasound source as shown in Fig. 1 in the paper, responsible for generating two focal points, has been optimized using the acoustic contrast control (ACC) method [12, 13], which enables adjustments to both amplitude and phase. As evident in Figs. S4(iv), this approach significantly mitigated the spurious lobe.
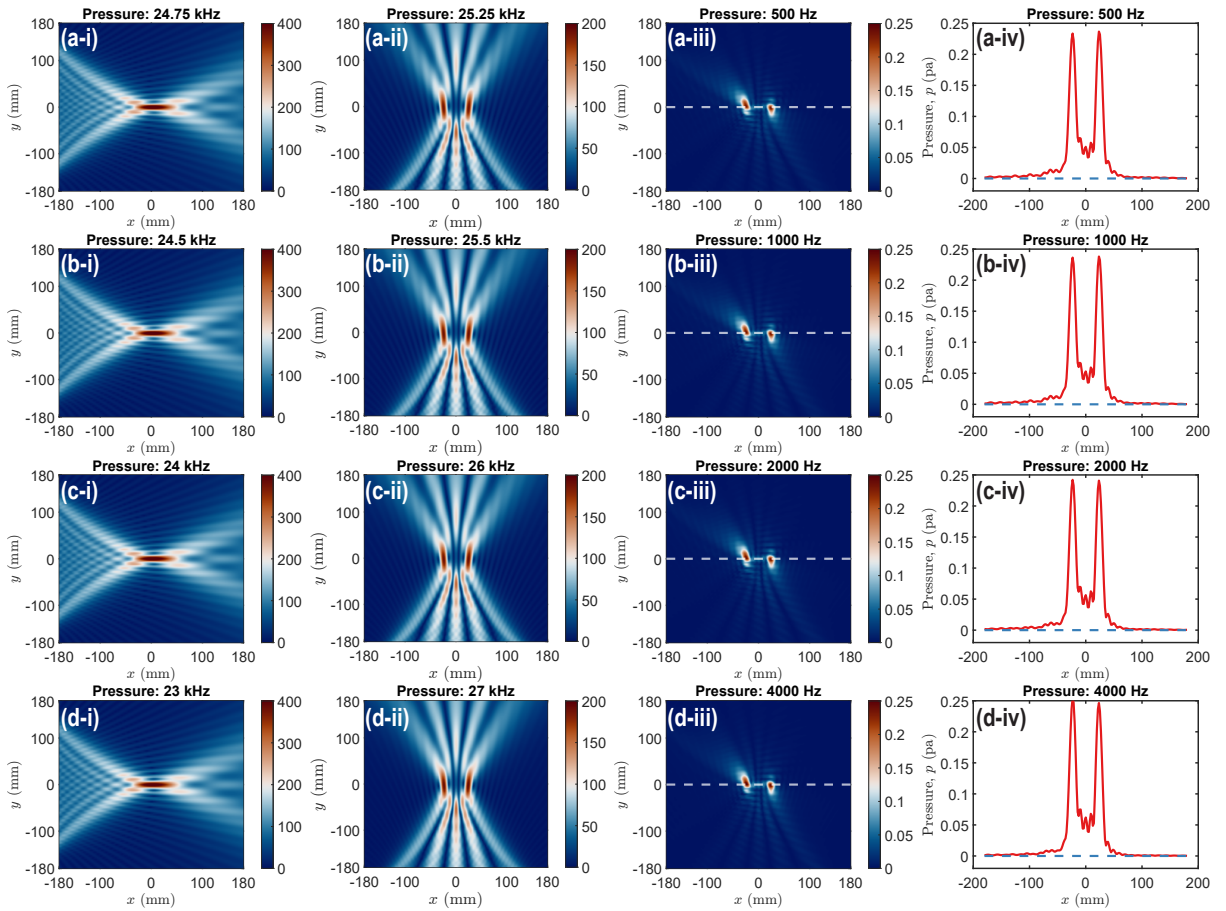

Figure S4: The performance of deep subwavelength focusing using the proposed local-nonlinearity-based technique by optimizing both amplitude and phase distributions. The 2D pressure distributions calculated by MATLAB using Eq. (S6) at (i) lower and (ii) higher ultrasound frequencies generating one-focal-point and two-focal-point ultrasound fields, respectively. (iii) The 2D pressure distributions of the DFW calculated by MATLAB using Eq. (1) in the paper. (iv) The sound pressure distribution along the dashed line $x = 0$ denoted in (iii). The DFW frequencies are 500 Hz, 1000 Hz, 2000 Hz, and 4000 Hz in (a), (b), (c), and (d), respectively. The focal distance is set as $D = 0.2\,\mathrm{m}$. ——— , with local effects; - - - , with only cumulative effects.

Furthermore, it is worth noting that the proposed local-nonlinearity-based technique remains applicable for wideband signals. While Fig. 4 in the paper showcases measured results spanning from 200 Hz

to 500 Hz, we have extended these findings to include simulation results up to 4000 Hz, as illustrated in Fig. S4. The results reveal that the proposed local-nonlinearity-based technique continues to generate two main lobes at ± 25 mm, maintaining its deep subwavelength resolution of less than the DFW wavelength.

5.2 Performance with the focal distance set to $D > \lambda$

The physical mechanism behind our proposed approach does not rely on evanescent waves in the near field. Instead, it capitalizes on the high resolution of ultrasound waves to overcome the diffraction limit when generating the locally generated DFW. To illustrate this, we presented the simulation results in Fig. S5, where the focal distance is set to 0.7 m, exceeding one wavelength at 500 Hz (0.68 m). Notably, we still observe the presence of two focal points with a deep subwavelength separation of 50 mm, equivalent to 0.07λ. It is worth noting that the main lobe width has expanded compared to the scenario where the focal distance is only 0.2 m, as shown in Fig. S4.
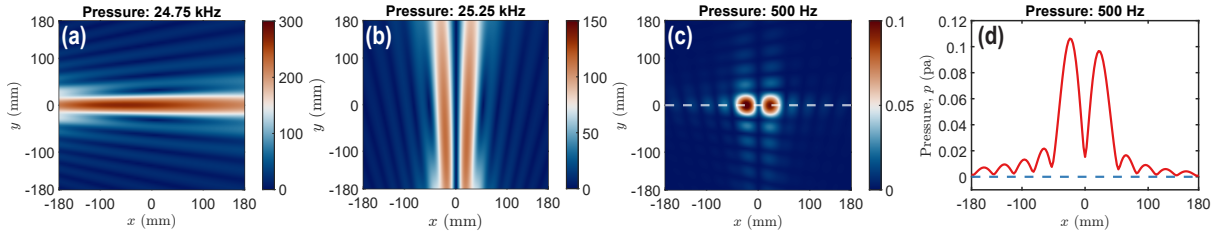

Figure S5: The 2D pressure distributions at (a) 24.75 kHz and (b) 25.25 kHz, respectively, for (a) a one-focal-point ultrasound field generated by the source placed on the left and (b) a two-focal-point ultrasound field generated by the source placed on the bottom. (c) The 2D pressure distribution of the DFW at 500 Hz, resulted from the local nonlinear interaction of waves at the two carrier frequencies. (d) The pressure distribution at 500 Hz along the dashed line denoted in Fig. S5(c). The focal distance is set as $D = 0.7$ m $> \lambda$. ——, with local effects; - - -, with only cumulative effects.

When the focal distance is extended to 2 m, which is larger than the wavelength of 1.715 m at 200 Hz, it becomes impossible to generate two distinguishable focal points using a source with a size of $a = 0.156$ m, as this size is only 0.09λ. Nonetheless, if the aperture size is doubled to $a = 0.312$ m (equivalent to 0.18λ), the simulation results presented in Fig. S6 demonstrate that two focal points with deep subwavelength resolution of 50 mm, corresponding to 0.03λ, can still be observed. Furthermore, in Fig. S4(d), we present simulation results with the focal point set at 0.2 m, but the DFW frequency is 4000 Hz (with a wavelength of 86 mm). Figure S4(d-iv) illustrates that deep subwavelength focusing can be achieved even at a focal distance of 2.33 wavelengths. In conclusion, our proposed physical mechanism relies on local nonlinearity rather than evanescent waves. This unique feature allows for the realization of deep subwavelength focusing even beyond one wavelength of the DFW, a capability that is not achievable in linear acoustics.

6 Performance of acoustic focusing using a conventional parametric array

Instead of orthogonal beams used in the paper, the combination of two collinear intensive ultrasound beams is referred to as a "parametric array" [7], as discussed in Sec. 1. In Fig. S7, we present the performance of this system in generating two focal points. Figures S7(i) and (ii) display the 2D pressure distributions calculated using MATLAB at 24.75 kHz and 25.25 kHz, respectively, when utilizing the focusing phase profile from Eq. (S5). Figure S7(iii) shows 2D pressure distribution of the DFW and
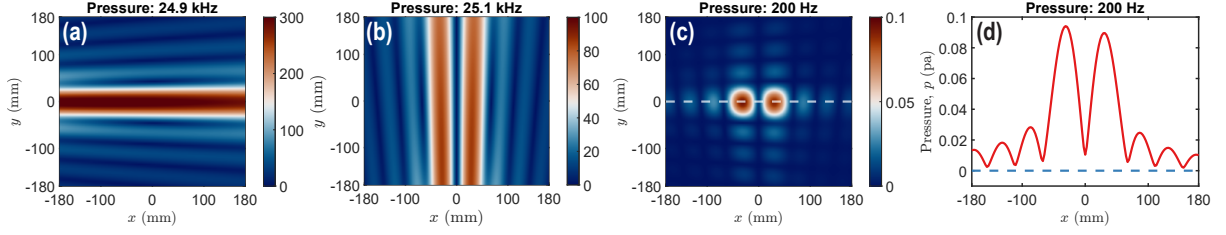
Figure S6: The 2D pressure distributions at (a) 24.9 kHz and (b) 25.1 kHz, respectively, for (a) a one-focal-point ultrasound field generated by the source placed on the left and (b) a two-focal-point ultrasound field generated by the source placed on the bottom. (c) The 2D pressure distribution of the DFW at 200 Hz, resulted from the local nonlinear interaction of waves at the two carrier frequencies. (d) The pressure distribution at 200 Hz along the dashed line denoted in Fig. S6(c). (e–h) Comparison of the results obtained using the conventional parametric array. The focal distance is set as $D = 2\,\text{m} > \lambda$. The source size is set as $a0.312\,\text{m}$. ⎯⎯, with local effects; - - -, with only cumulative effects.

Fig. S7(iv) shows the pressure distribution along the dashed line at $x = 0$. It can be observed that two focal points are formed at $y = \pm 25\,\text{mm}$ at 500 Hz, 1000 Hz, and 2000 Hz, except at 4000 Hz. Although two pressure peaks are generated at the focal points $(0, \pm 25\,\text{mm})$ below 3000 Hz, they cannot be easily distinguished due to the presence of three peaks with an amplitude larger than half of the amplitude of the main lobe.
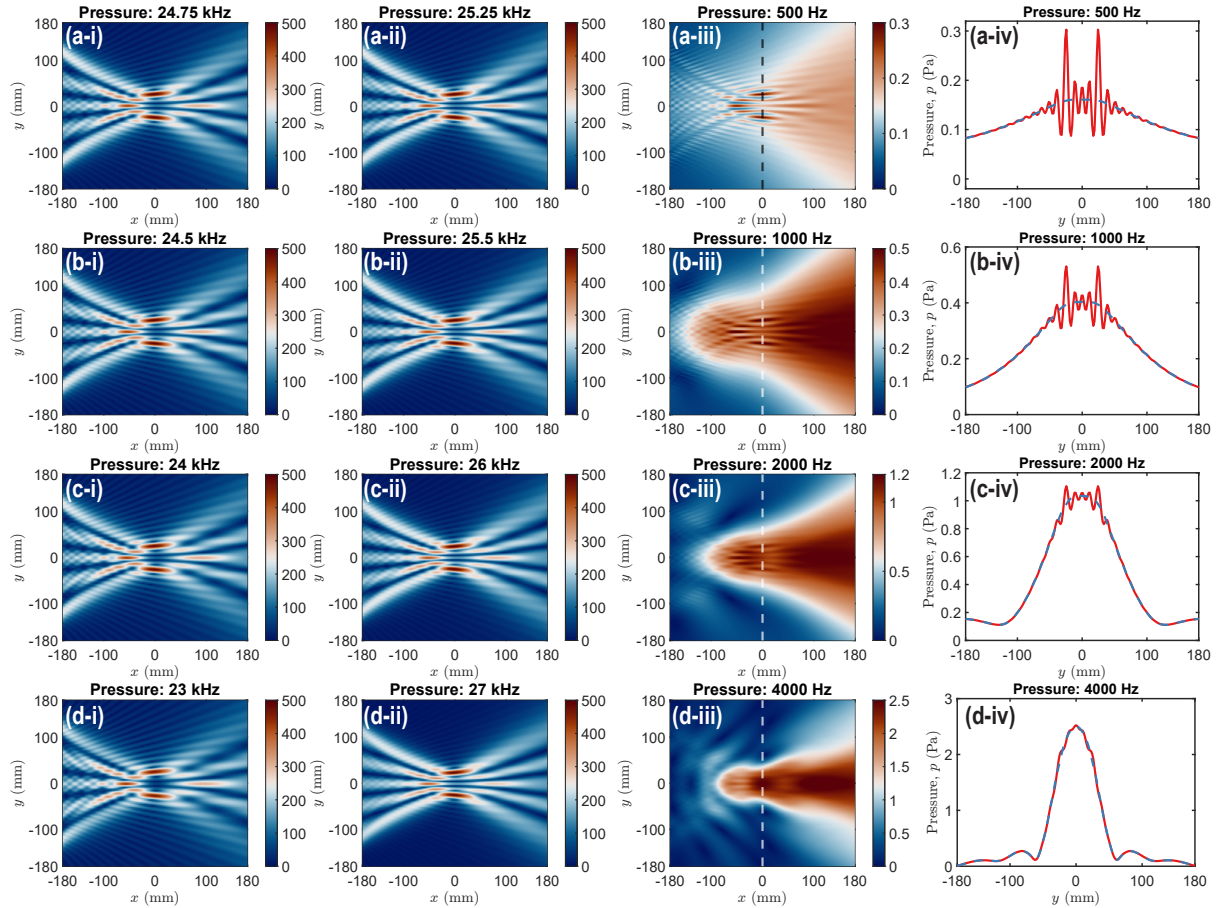

Figure S7: The performance of acoustic focusing using the conventional parametric array technique by setting a focusing phase distribution. The 2D pressure distributions calculated by MATLAB using Eq. (S6) at (i) lower and (ii) higher ultrasound frequencies generating two-focal-point ultrasound fields. (iii) The 2D pressure distributions of the DFW calculated by MATLAB using Eq. (1) in the paper. (iv) The sound pressure distribution along the dashed line $x = 0$ denoted in (iii). The DFW frequencies are 500 Hz, 1000 Hz, 2000 Hz, and 4000 Hz in (a), (b), (c), and (d), respectively. The focal distance is set as $D = 0.2\,\text{m}$. ⎯⎯, with local effects; - - -, with only cumulative effects.

Figure S8 displays the results obtained using the conventional parametric array technique, where both amplitude and phase distributions have been optimized. When compared to Fig. S7(iv), it is observed that there is a slight improvement in focusing performance along the line $x = 0$. However, this improvement is obtained at the cost of the pressure in the region $x > 0$ becoming significantly larger, rendering it unsuitable for subwavelength focusing. In conclusion, when dealing with a parametric array employing two collinear primary waves, the cumulative nonlinear effects prove too formidable to eliminate completely, even when optimizing both amplitude and phase distributions of the sources.
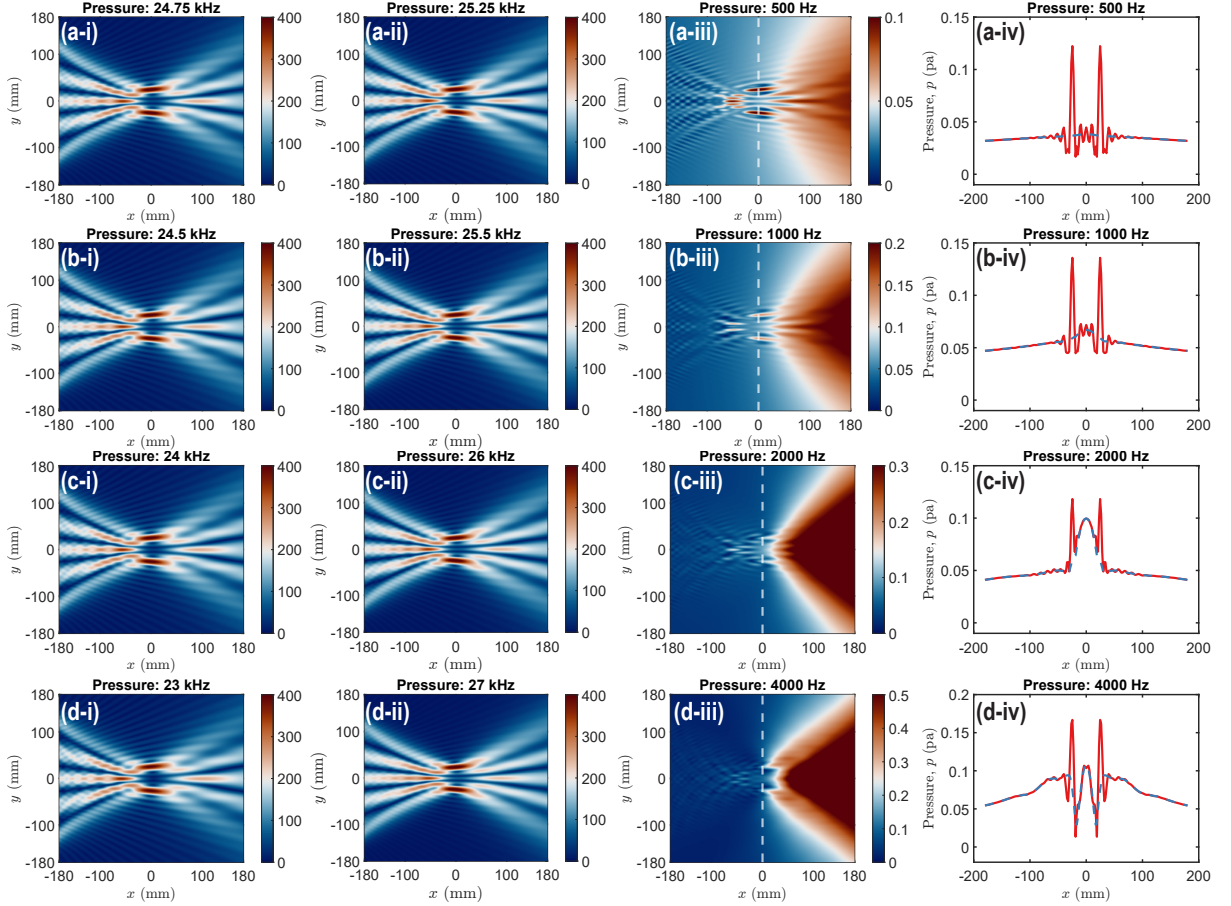

Figure S8: The performance of acoustic focusing using the conventional parametric array technique by optimizing both amplitude and phase distributions. The 2D pressure distributions calculated by MATLAB using Eq. (S6) at (i) lower and (ii) higher ultrasound frequencies generating two-focal-point ultrasound fields. (iii) The 2D pressure distributions of the DFW calculated by MATLAB using Eq. (1) in the paper. (iv) The sound pressure distribution along the dashed line $x = 0$ denoted in (iii). The DFW frequencies are 500 Hz, 1000 Hz, 2000 Hz, and 4000 Hz in (a), (b), (c), and (d), respectively. The focal distance is set as $D = 0.2\,\mathrm{m}$. ——— , with local effects; - - - , with only cumulative effects.

References

[1] M. Červenka and M. Bednařík, "A versatile computational approach for the numerical modelling of parametric acoustic array," *J. Acoust. Soc. Am.*, vol. 146, no. 4, pp. 2163–2169, 2019.

[2] B. Hamilton and S. Bilbao, "Time-domain modeling of wave-based room acoustics including viscothermal and relaxation effects in air," *JASA Express Letters*, vol. 1, no. 9, p. 092 401, Sep. 2021.

[3] A. D. Pierce, *Acoustics: An Introduction to Its Physical Principles and Applications*, 3rd. Cham, Switzerland: Springer Nature, 2019.

[4] S. I. Aanonsen, T. Barkve, J. N. Tjøtta, and S. Tjøtta, "Distortion and harmonic generation in the nearfield of a finite amplitude sound beam," *J. Acoust. Soc. Am.*, vol. 75, no. 3, pp. 749–768, 1984.

[5] J. Zhong, R. Kirby, and X. Qiu, "The near field, Westervelt far field, and inverse-law far field of the audio sound generated by parametric array loudspeakers," *J. Acoust. Soc. Am.*, vol. 149, no. 3, pp. 1524–1535, 2021.

[6] J. Zhong, R. Kirby, M. Karimi, and H. Zou, "A cylindrical expansion of the audio sound for a steerable parametric array loudspeaker," *J. Acoust. Soc. Am.*, vol. 150, no. 5, pp. 3797–3806, 2021.

[7] W.-S. Gan, J. Yang, and T. Kamakura, "A review of parametric acoustic array in air," *Appl. Acoust.*, vol. 73, no. 12, pp. 1211–1219, 2012.

[8] P. J. Westervelt, "Parametric acoustic array," *J. Acoust. Soc. Am.*, vol. 35, no. 4, pp. 535–537, 1963.

[9] K. G. Foote, "Reflections on "Parametric acoustic array," source of virtual-array sonars," *J. Acoust. Soc. Am.*, vol. 150, no. 1, R1–R2, Jul. 1, 2021.

[10] K. Melde, A. G. Mark, T. Qiu, and P. Fischer, "Holograms for acoustics," *Nature*, vol. 537, no. 7621, pp. 518–522, Sep. 22, 2016.

[11] L. W. Schmerr Jr, *Fundamentals of Ultrasonic Phased Arrays*. New York: Springer, 2014.

[12] J.-W. Choi and Y.-H. Kim, "Generation of an acoustically bright zone with an illuminated region using multiple sources," *J. Acoust. Soc. Am.*, vol. 111, no. 4, pp. 1695–1700, 2002.

[13] J.-H. Chang, C.-H. Lee, J.-Y. Park, and Y.-H. Kim, "A realization of sound focused personal audio system using acoustic contrast control," *J. Acoust. Soc. Am.*, vol. 125, no. 4, pp. 2091–2097, Apr. 2009.